Supplementary information for

Transient Potential Amplification in Dynamically Operated Electrochemical Systems

Huili Zeng *et al*.

Corresponding Author: Xin Xiao, xinxiao@zju.edu.cn; Baoliang Chen, blchen@zju.edu.cn; Weilai Yu, weilai.yu@utoronto.ca.

The PDF file includes:

Contents

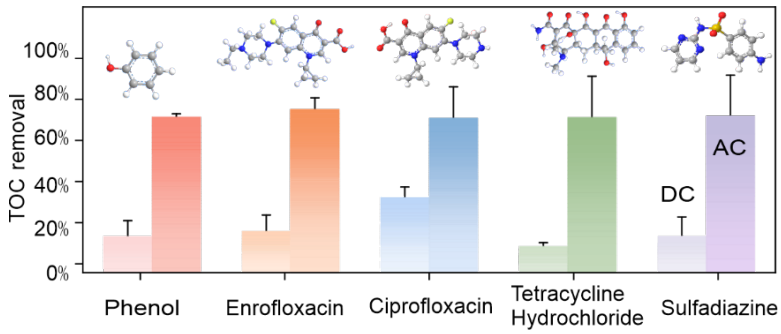

Supplementary Fig. 1 A comparison of TOC removal percentage for different types of organic chemicals in the FES system with (AC, ± 3 V cell voltage, 0.01 Hz, 50% duty cycle, dark color) and without voltage switch (DC, 3 V, light color). Condition: FES, CF electrode, 0.1 mol L^{-1} KCl+10 mg L^{-1} Phenol,

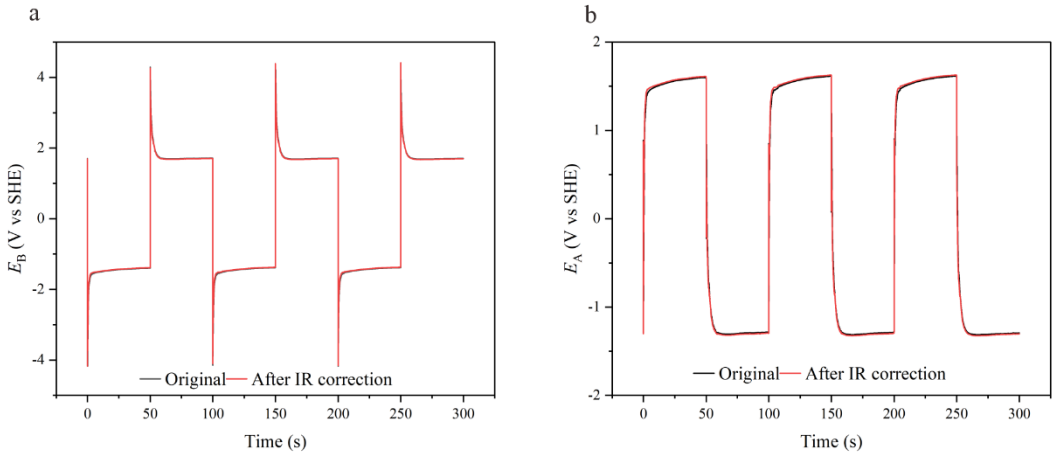

Supplementary Fig. 2 The influence of Internal Resistance Compensation (IR correction) for the outflow electrode (a) and inflow electrode (b). Note that the typical condition is carbon felt (CF) electrode, FES, KCl electrolytes, ± 3V, 0.01 Hz. The influence of the IR correction conditions on the data was compared. Due to the extremely low resistance of FES, there was almost no difference between the data before and after IR correction. Therefore, no further IR correction was performed on the subsequent data.

Supplementary Note 1. APEX behavior at varied condition

In the flow-through electrode system (FES), the APEX behavior is observed for all investigated electrode materials. However, its intensity is closely associated with the electrode reaction pathways and the interfacial microenvironment. Among the materials examined in this study, carbon-based electrodes were identified as the most suitable choice. Notably, variations in electrolyte composition did not significantly influence the intensity of APEX. Comparative analysis across different electrolyzers configurations revealed a pronounced dependence of APEX behavior on cell architecture. The strongest APEX response was observed in the FES, whereas the weakest was detected in the single-chamber cell. In contrast, both the flow-by cell and the H-cell exhibited prolonged positive APEX signals, which can be attributed to the presence of a proton exchange membrane that modulates interfacial ion transport and consequently extends the duration of the positive APEX component.

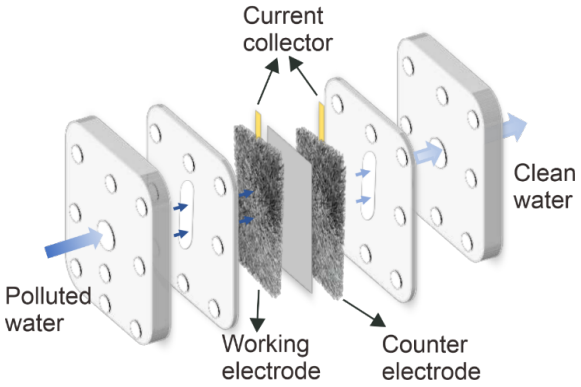

Supplementary Fig. 3 Schematic of the FES.

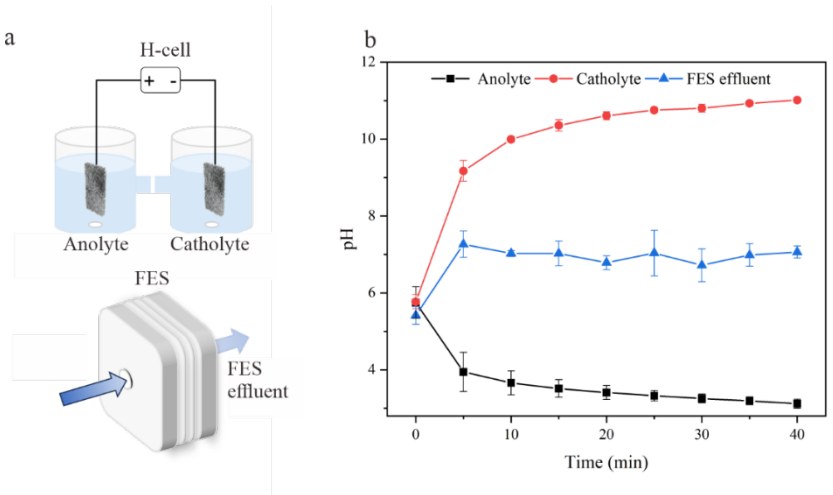

Supplementary Fig. 4 pH variation in both compartments of H-cell and FES effluent.

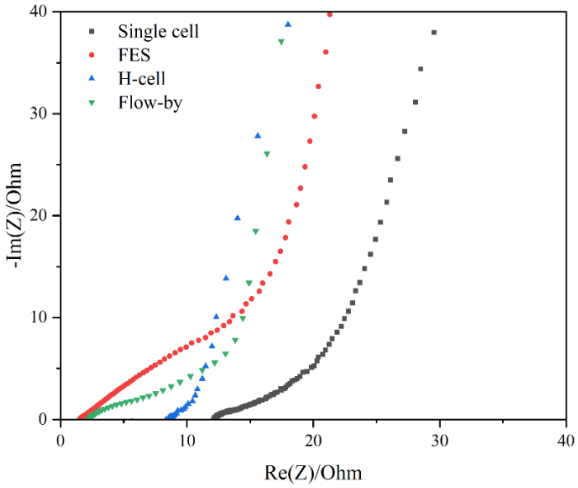

Supplementary Fig. 5 Electrochemical impedance spectroscopy (EIS) spectra of the single-chamber cell, FES, H-cell and flow-by cell.

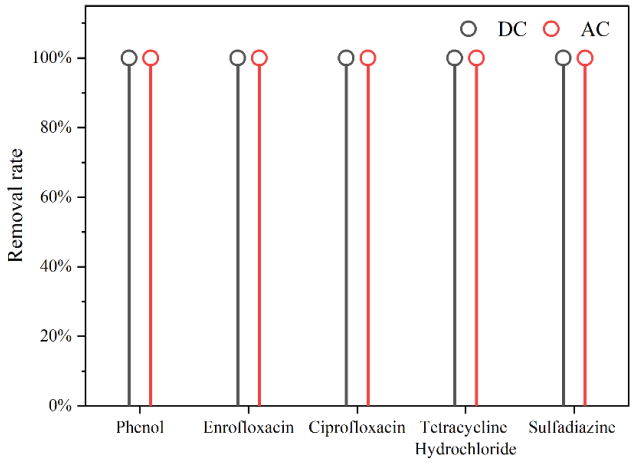

Supplementary Fig. 6 The concentration removal rate for organic pollutants in the FES system without voltage switch (DC, black color) and with voltage switch (AC, red color) condition.

Supplementary Note 2. Diffusion time calculation

During electrochemical processes, compounds initially remain uniformly dispersed in the electrolyte and do not participate in direct interfacial electron transfer. However, as they traverse the diffusion layer and accumulate at the electrode-electrolyte interface, they become actively involved in interfacial reactions. Therefore, for electron-neutral compounds, their diffusion coefficient and the thickness of the diffusion layer at the electrode interface collectively determine the minimum time required for their participation in the electrochemical process. This duration is also key to whether alternating current conditions can achieve enhanced removal efficiency.

The calculation formula for diffusion time is as follows：

$$t = \frac{\delta^2}{2D}$$

δ is the thickness of the diffusion layer，D is diffusion coefficient.

$\delta = 10\ \mu m$ is calculated by COMSOL[1] as shown in Supplementary Fig. 7. The second difference approximation is used to solve the transient diffusion model based on Fick's second law. The detailed parameters are shown in Supplementary Table 1.

And for phenol, its diffusion coefficient is approximately[2,3] D =10^{-9} m^2s^{-1}. Therefore, the diffusion time can be calculated as 0.05 s, the corresponding frequency is 10 Hz.

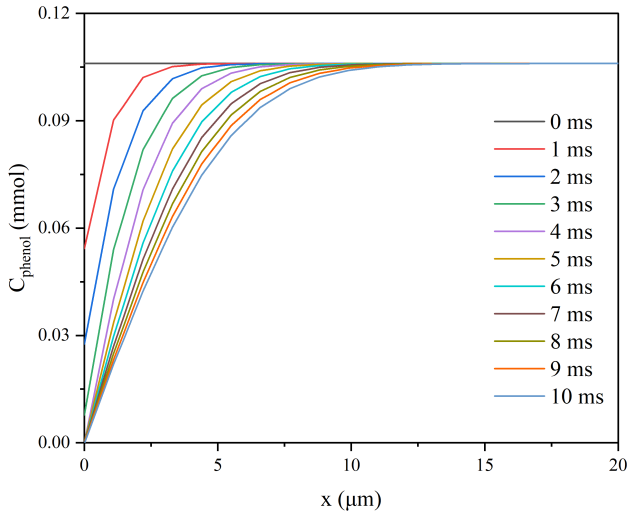

Supplementary Fig. 7 Simulated phenol concentration at the anode surface.

Supplementary Note 3. Multiphysics simulation

The electrolytic cell was configured with homogeneous porous electrodes for both the anode and cathode, separated by a filter membrane. The electrolyte enters from the left boundary, passes through the porous electrodes, and flows across the cell under the driving force of the applied flow rate, as illustrated in Supplementary Fig. 8. The simulations of pH distribution in a 2D domain were performed using the COMSOL Multiphysics package based on a finite-element-based solver, with a focus on the effects of alternating frequency and flow rate. The model employed the Tertiary Current Distribution interface supporting a supporting electrolyte, with potentials in the porous electrodes and electrolyte calculated based on charge conservation and Ohm's law. Species transport in the electrolyte was described by the Nernst-Planck equation, incorporating diffusion, electromigration, and convection. An alternating potential was applied directly to the porous electrodes, with the anode and cathode driven by anti-phase alternating square-wave voltages of ± 1.5 V vs. Ag/AgCl, without setting a ground potential. The electrode current density at the electrode-electrolyte interface was modeled using the Butler-Volmer equation. In addition, the influence of the electric double layer was considered in the pH simulation, with corresponding experimental results shown in Supplementary Fig. 34. And the detailed parameters are shown in Supplementary Table 2.

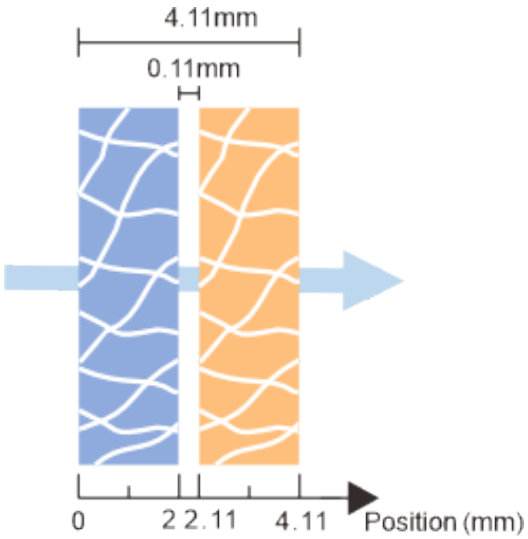

Supplementary Fig. 8 Schematic diagram of the model simulated by COMSOL.

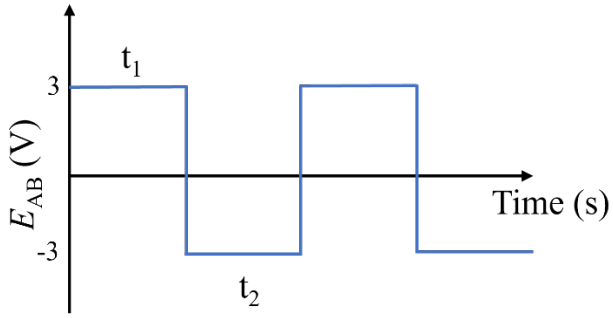

Supplementary Fig. 9 Schematic diagram of square wave alternating current

Supplementary Note 4. Optimization of AC frequency and duty cycle

For AC), Frequency and Duty cycle are calculated as:

$$Frequency = \frac{1}{t_1+t_2}, \quad Duty\ cycle = \frac{t_1}{t_1+t_2}$$

During process optimization, the effects of AC frequency (Supplementary Figs. 10-11) and duty cycle (Supplementary Figs. 12-13) were systematically evaluated. Under DC conditions, phenol was primarily converted into larger intermediates such as hydroquinone and p-benzoquinone, which retained significant biological toxicity. In contrast, under AC conditions, phenol was largely transformed into inorganic carbon and small organic acids with negligible environmental toxicity. Deep mineralization of phenol was achieved at low frequencies (<1 Hz), whereas medium frequencies (10-50 Hz) led to a marked decrease in mineralization efficiency, corresponding to the calculated diffusion time of phenol molecules through the diffusion layer (Supplementary Note 3). These results reveal the insufficient understanding of frequency in previous work (Supplementary Table 3), highlighting that incomplete evaluation of frequency parameters constrains the performance and broader application of AC electrochemical systems.

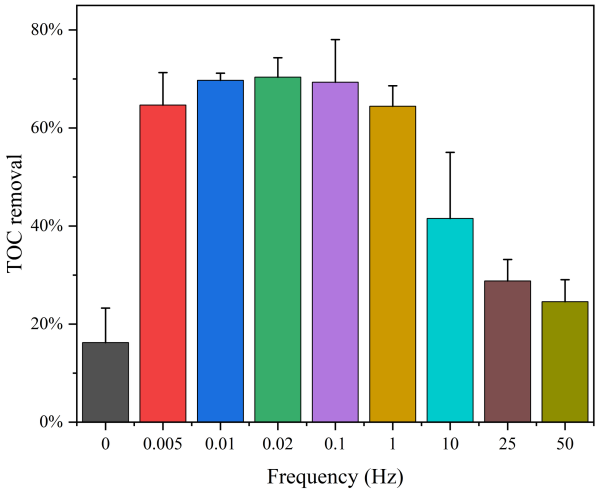

Supplementary Fig. 10 Phenol mineralization under AC at various frequencies (Square wave, 50% duty cycle; 0 Hz refers to constant 3 V).

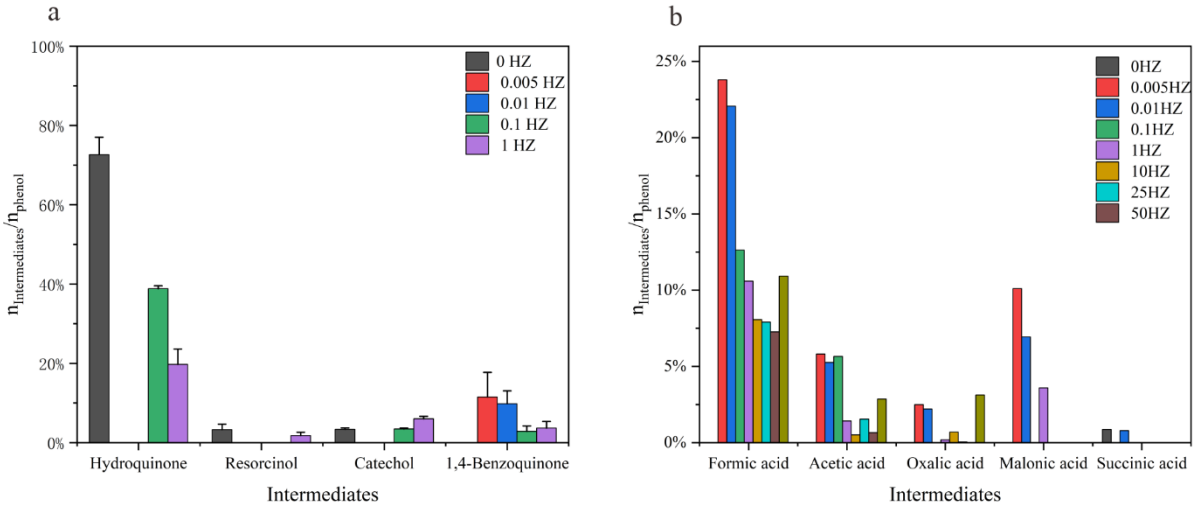

Supplementary Fig. 11 Phenol products under AC at various frequencies. (a) Detected by liquid chromatography (LC); (b) Detected by ion chromatography (IC). (The vertical coordinate represents the number of molecules of the product divided by the number of molecules of the phenol.)

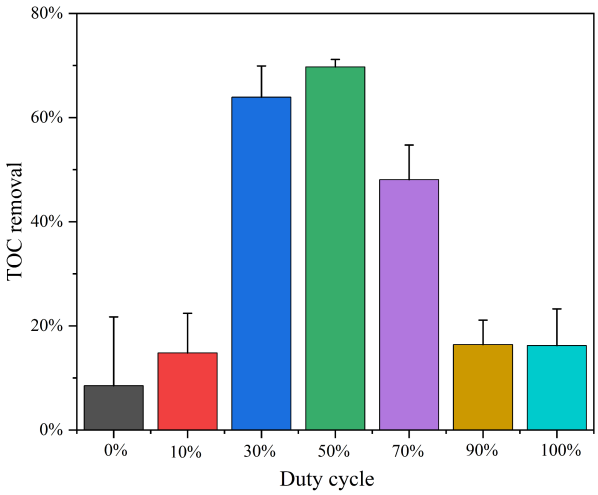

Supplementary Fig. 12 Phenol mineralization under AC at various duty cycles (frequency = 0.01 Hz).

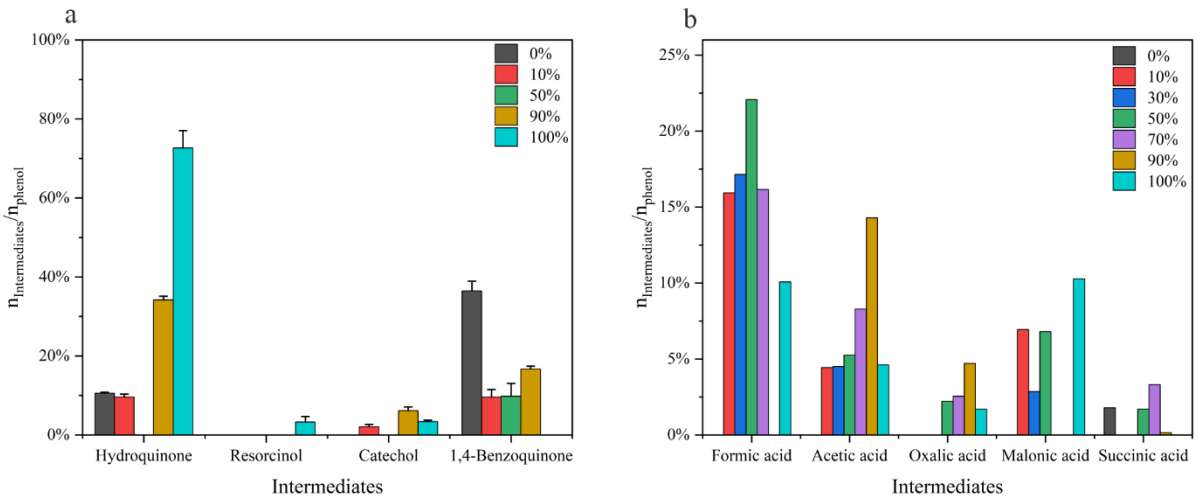

Supplementary Fig. 13 Phenol products under AC at various duty cycles. Detected by LC; (b) Detected by IC. ($\eta_{intermediates}/\eta_{phenol}$： The vertical coordinate represents the number of molecules of the product divided by the number of molecules of the phenol.)

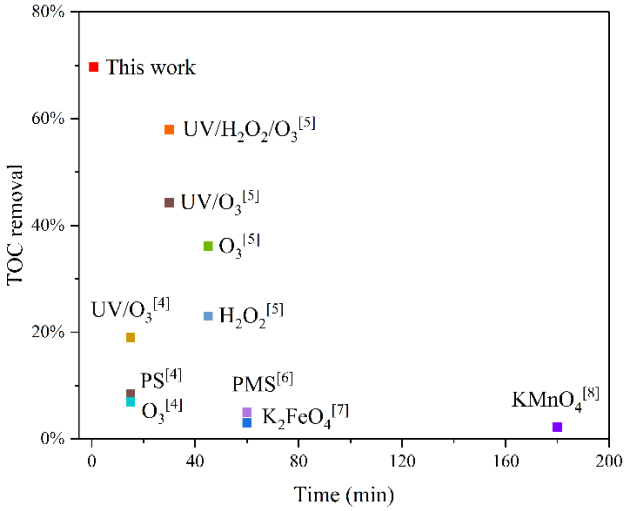

Supplementary Fig. 14 Phenol mineralization by different chemical oxidants without catalyst addition[4-8].

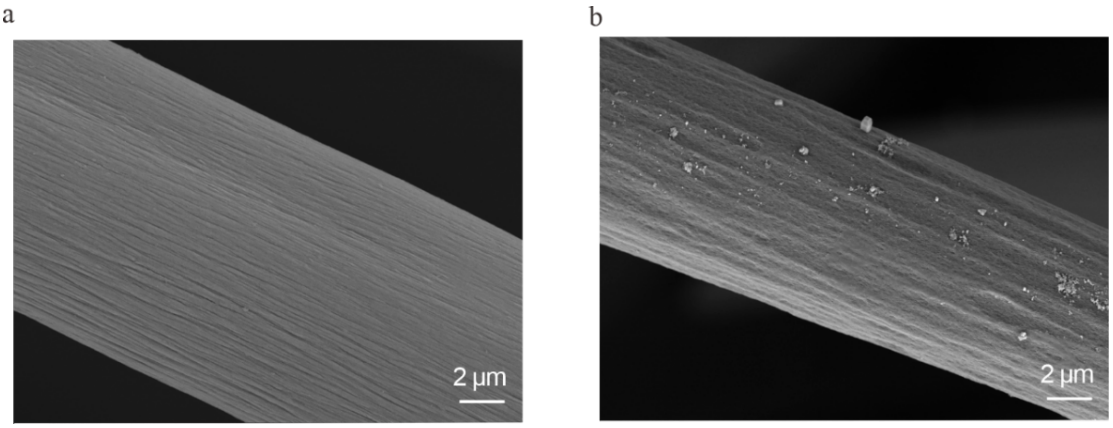

Supplementary Fig. 15 SEM images of carbon felt electrodes before (**a**) and after (**b**) 500 h long-term testing.

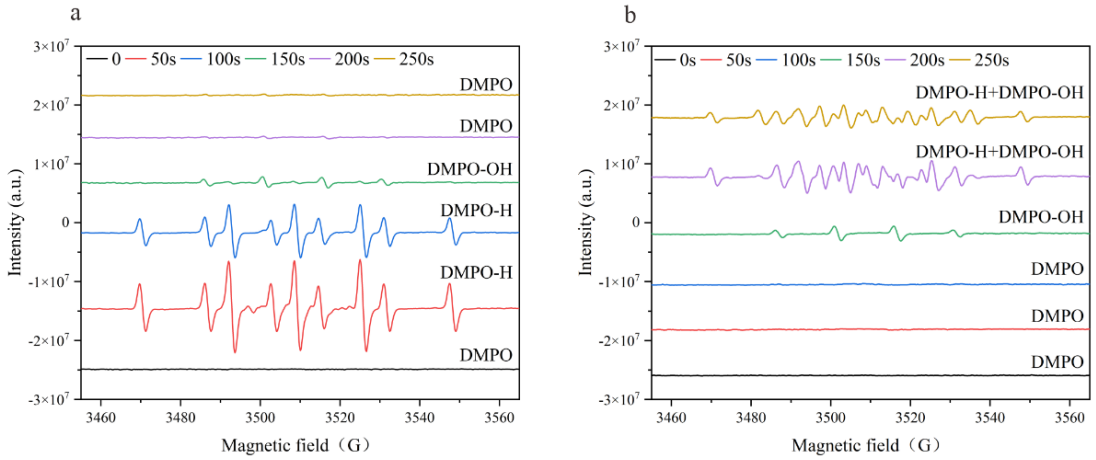

Supplementary Fig. 16 Electron Paramagnetic Resonance (EPR) spectroscopy. Conditions: 10 mmol L^{-1} DMPO, 0.1 mol L^{-1} KCl. (a) +3 V for 250 s, -3 V for 250 s, sampling every 100 s; (b) -3 V for 250 s, +3 V for 250 s, sampling every 100 s.

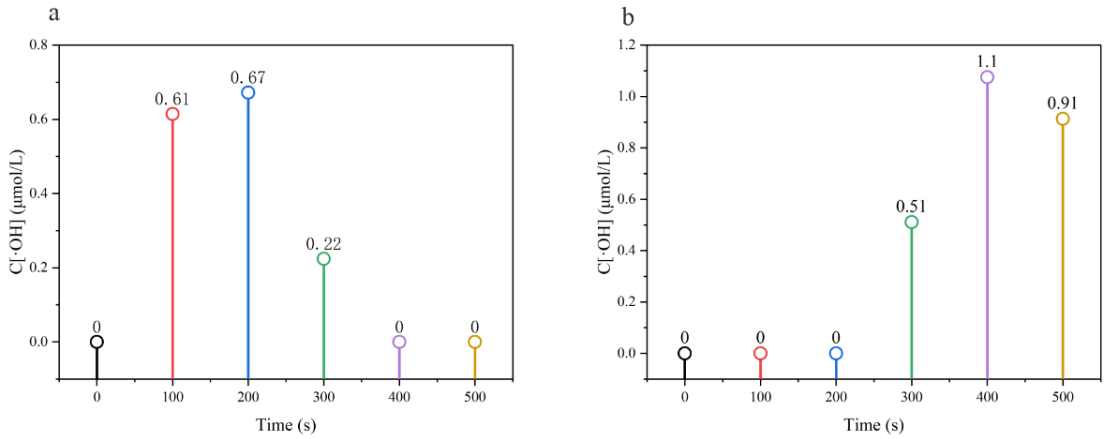

Supplementary Fig. 17 Hydroxyl radical scavenging experiment. Conditions: 1 g L^{-1} TPA, 0.1 mol L^{-1} KCl. (a) +3 V for 250 s, -3 V for 250 s, sampling every 100 s; (b) -3 V for 250 s, +3 V for 250 s, sampling every 100 s.

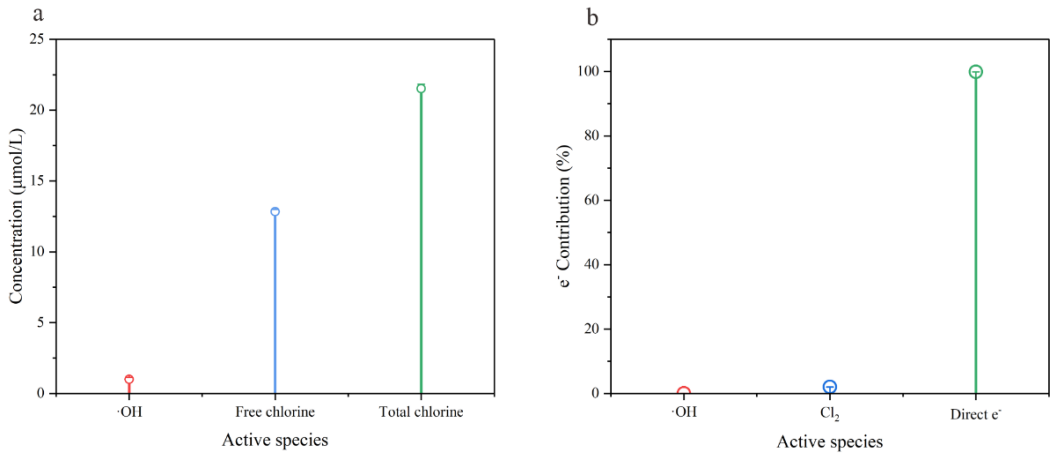

Supplementary Fig. 18 Quantification of active species. (a) Quantification of active species, where free chlorine and total chlorine were determined using DPD spectrophotometry; (b) The contribution of electrons provided by each active species.

Supplementary Note 5. Active species analysis

Considering the electron supply capacity of the system, direct charge transfer was therefore identified as the dominant reaction mechanism. In direct electro-oxidation processes, electrode interfacial behavior is critical.

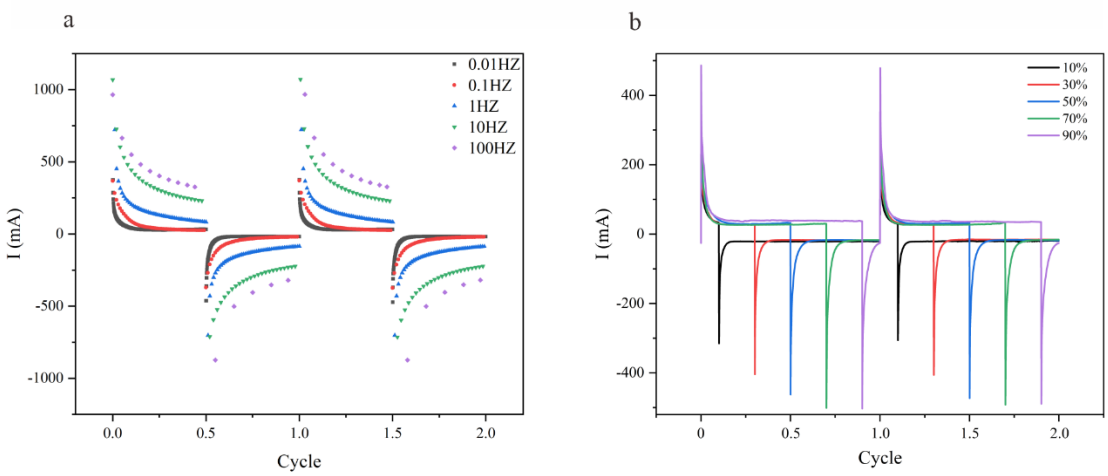

Supplementary Fig. 19 Current profiles under different alternating current. (a) at various frequencies; (b) at various duty cycles.

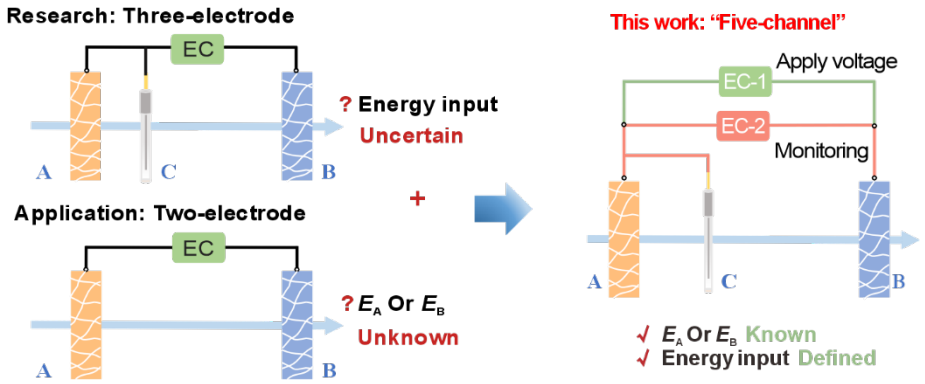

Supplementary Fig. 20 Schematic of the five-channel system. Two electrochemical workstations (EC-1, EC-2), among which EC-1 is used to supply voltage to the two electrodes, and EC-2 is used to monitor the voltage of the electrodes relative to the reference electrode.

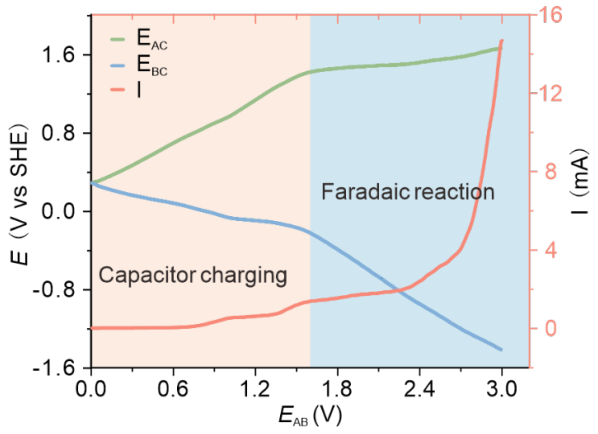

Supplementary Fig. 21 Potential distribution and current response during linear sweep voltammetry (LSV) scan in a two-electrode system.

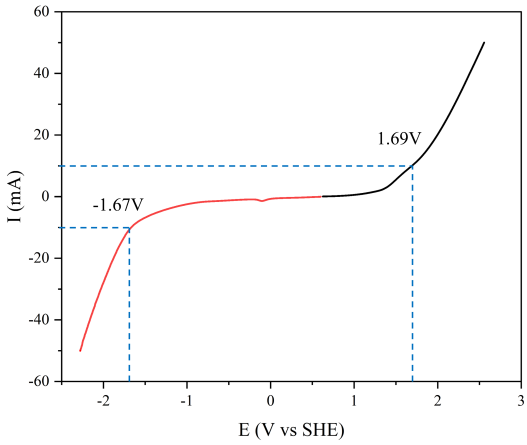

Supplementary Fig. 22 LSV of the carbon felt electrode. Condition: single-chamber cell with 0.1 mol L^{-1} KCl solution at a scan rate of 5 mV s^{-1}.

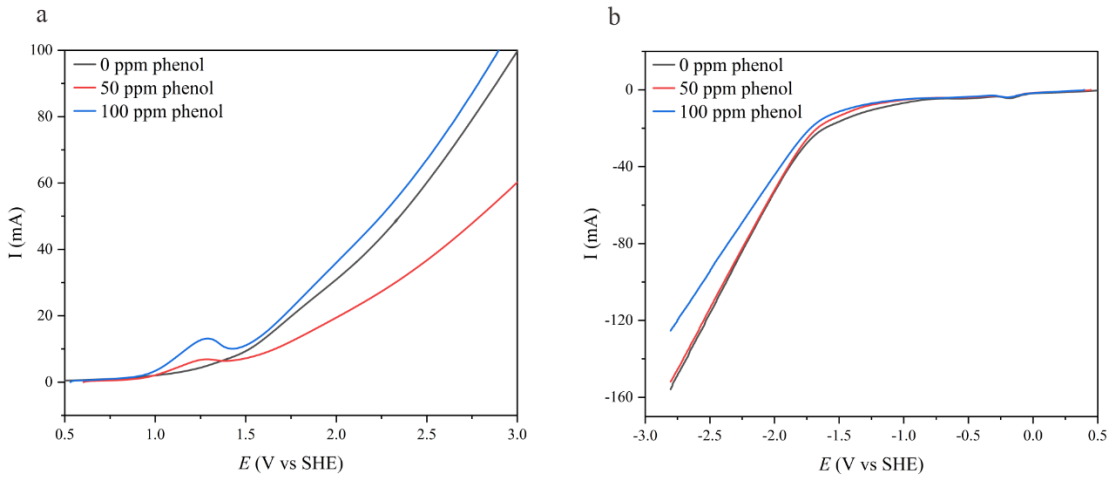

Supplementary Fig. 23 LSV of phenol. Single-chamber cell with 0.1 M KCl + phenol solution at a scan rate of 20 mV s^{-1}.

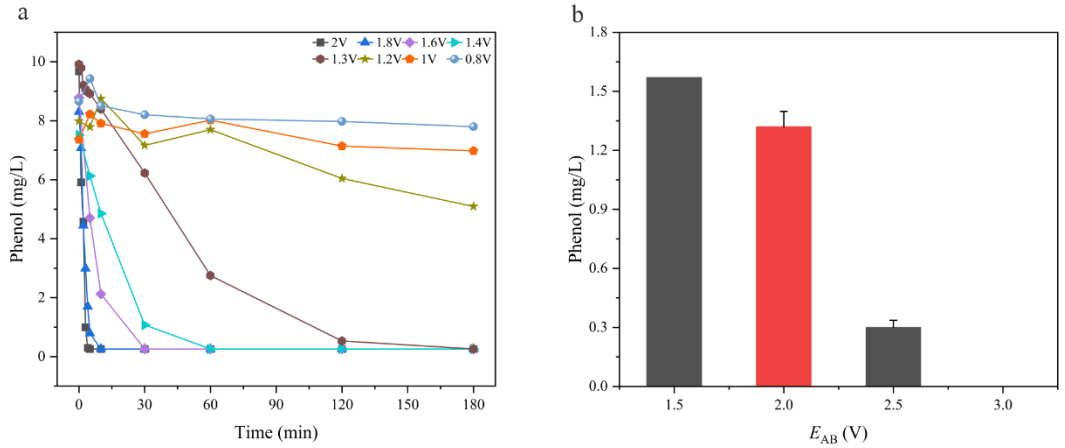

Supplementary Fig. 24 Phenol removal behavior at different voltages. (a) Kinetics of phenol removal at different oxidation potentials (H cell); (b) remained phenol concentrations at different two-electrode voltages (FES).

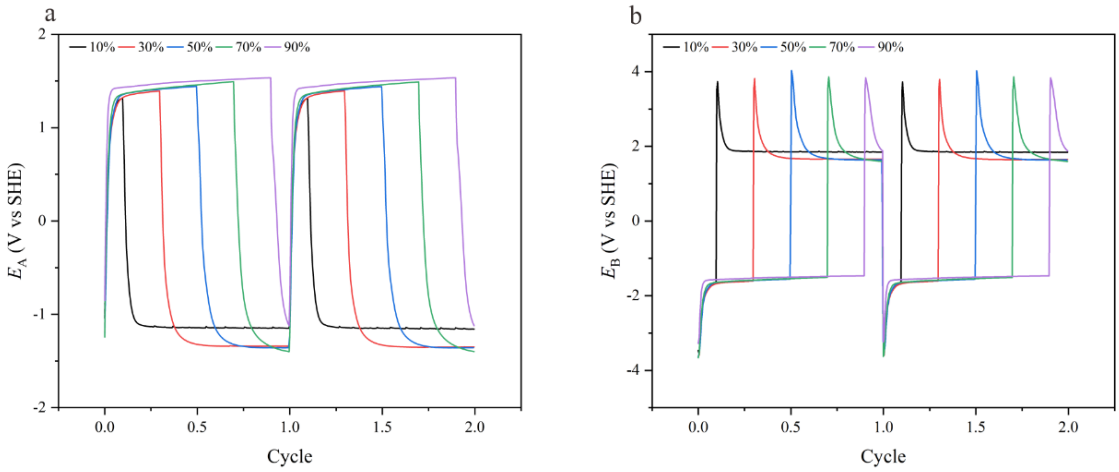

Supplementary Fig. 25 Electrode voltages at different duty cycles (cell voltage = ± 3V).

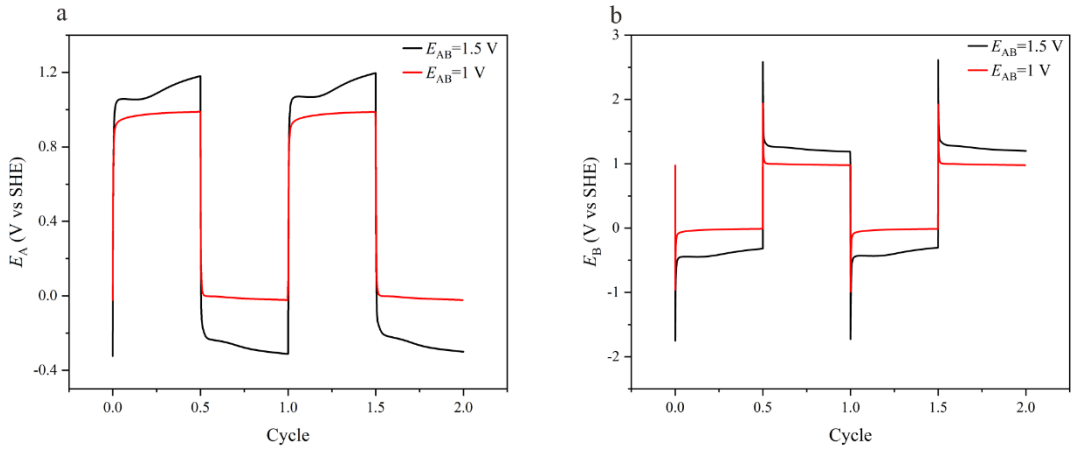

Supplementary Fig. 26 Electrode voltages at different applied voltages of (a) electrode A; (b) electrode B (frequency = 0.01 HZ, duty = 50%).

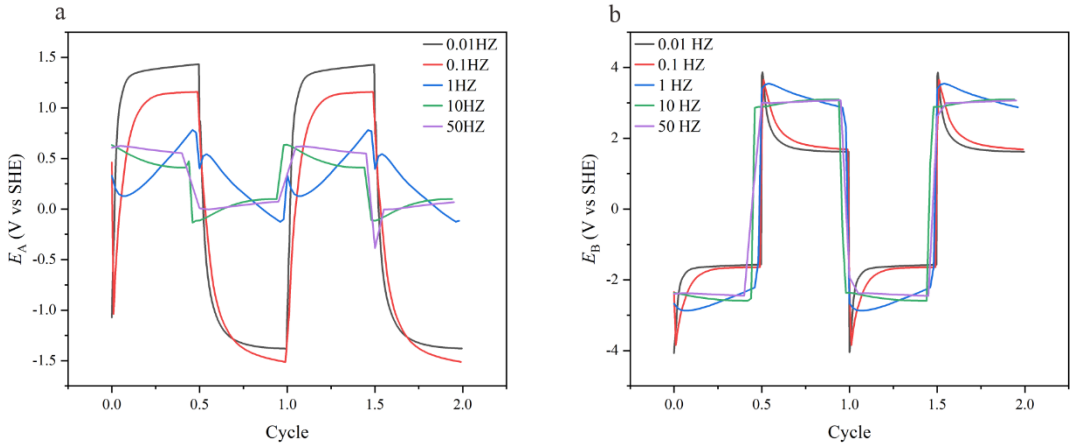

Supplementary Fig. 27 Electrode potential at different frequencies.

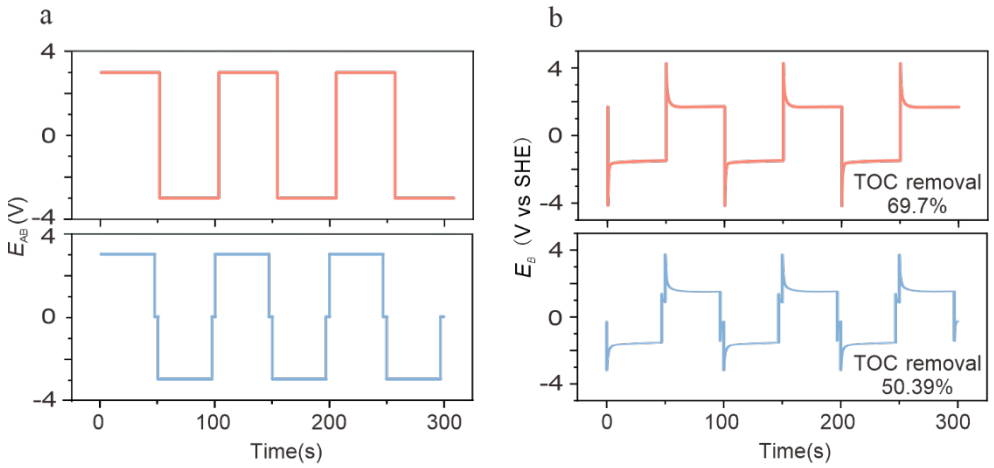

Supplementary Fig. 28 Experimental setup for short-circuit program (a) and (b) potential of B electrode.

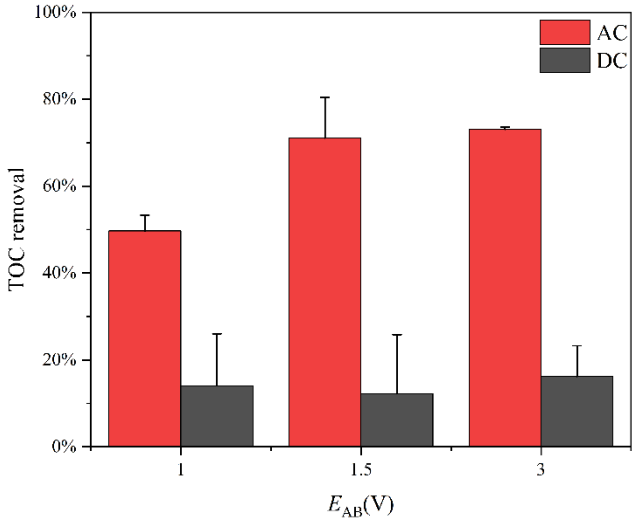

Supplementary Fig. 29 Phenol mineralization at different applied voltages.

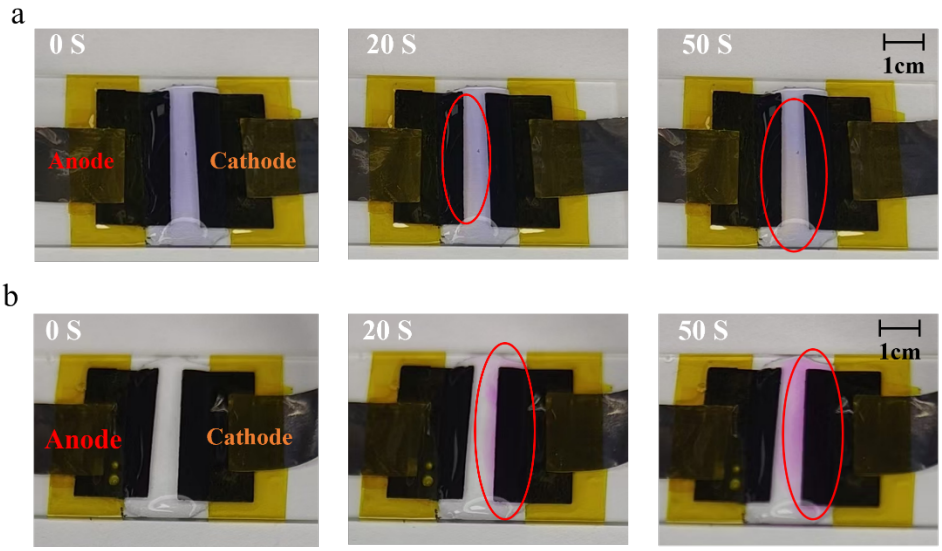

Supplementary Fig. 30 Visualization of pH distribution using acid-base indicators. Condition: 400 μL of 10 mg L^{-1} phenol + 0.1 M KCl + 5% purple litmus solution (a) or 2% phenolphthalein solution (b) at 3 V cell voltage.

Supplementary Note 6. Visualization of pH distribution

To visualize local pH variations at the electrode interface, purple litmus and phenolphthalein were used as acid-base indicators in a simple homemade electrolytic cell. Purple litmus changes from purple to red at pH < 5, indicating acidification near the anode during electrolysis. Phenolphthalein turns from colorless to red at pH > 8.2, revealing the formation of a local alkaline environment near the cathode.

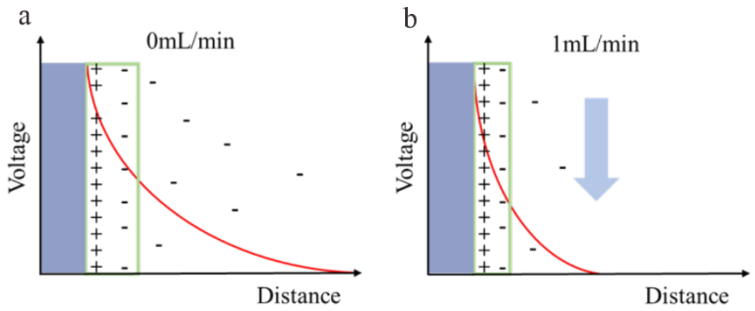

Supplementary Fig. 31 Schematic of diffusion layer thickness variation with flow rate.

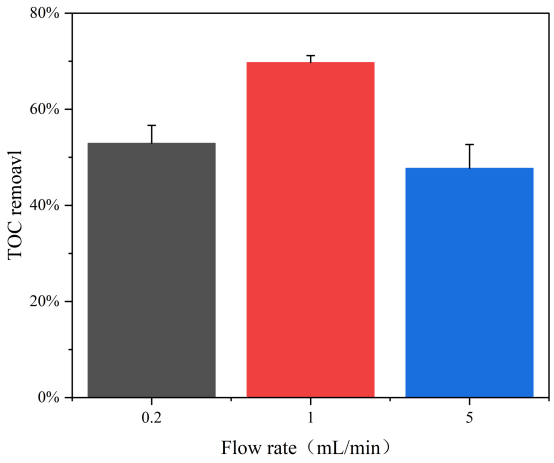

Supplementary Fig. 32 Phenol mineralization at different flow rates.

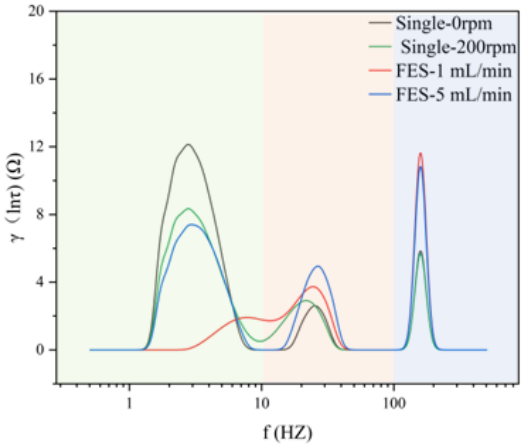

Supplementary Fig. 33 Distribution of relaxation times (DRT) analysis. Green region: Diffusion impedance; Red region: Molecular adsorption/desorption; Blue region: Direct charge transfer.

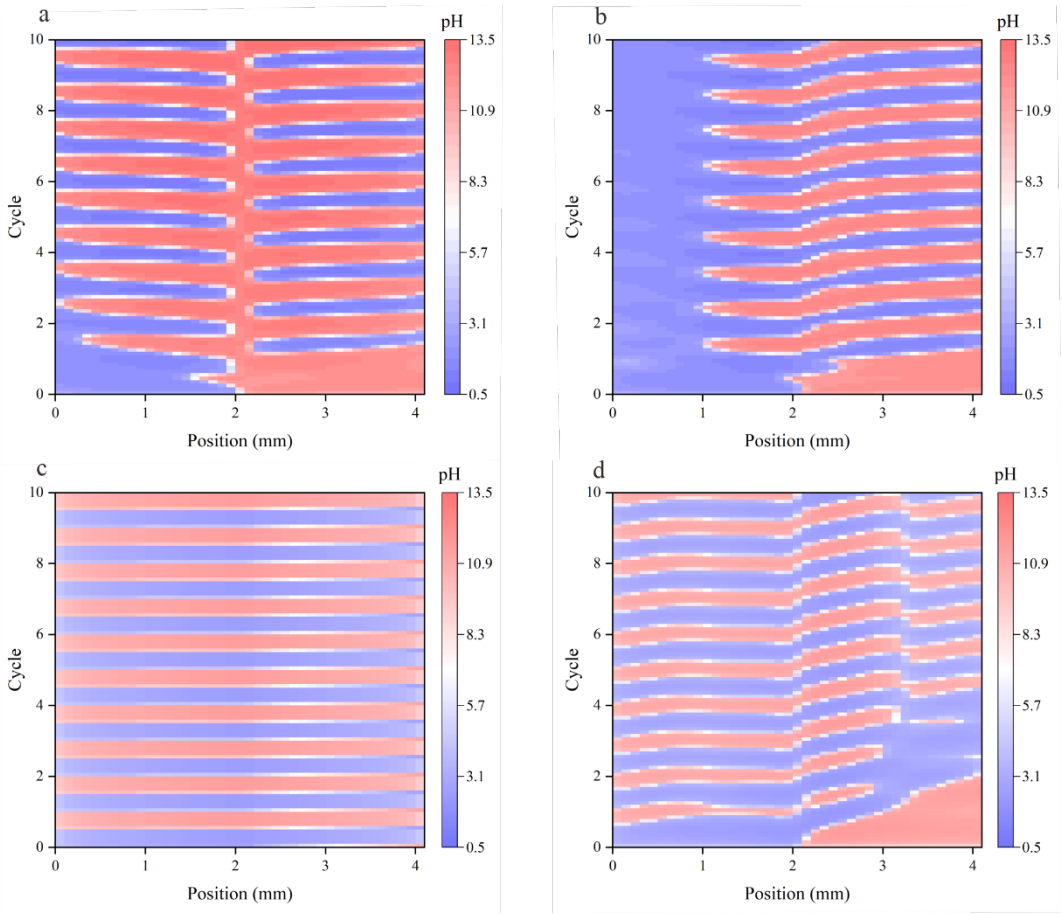

Supplementary Fig. 34 The pH distribution and variation simulated by COMSOL. The pH distribution at 0 ml·min^{-1}, 0.01 Hz (a) 0.2 ml·min^{-1}, 0.01Hz (b), 5 ml·min^{-1}, 0.01 Hz (c), 1 ml·min^{-1}, 0.1 Hz (d) in FES simulated by COMSOL.

Supplementary Note 7. The pH distribution and variation simulation

At higher frequencies, the electrolyte flow rate is insufficient to transport H^+/OH^- generated at electrode A to electrode B, resulting in distinct local environments at the two electrodes. When the electrode switching frequency is slower than the hydraulic retention time9, the pH inside the electrolytic cell tends to be consistent, which can eliminate the concentration polarization within the electrolytic cell and enhance the Faraday process. However, at excessively low frequencies, contaminants fail to desorb from electrode, which significantly reduces electrode effectiveness. Similarly, the flow rate changes the hydraulic retention time, also affects the pH distribution within the electrolytic cell. Therefore, only when the frequency matches the hydraulic retention time can the pH distribution within the electrolytic cell present a periodic pattern. If they do not match, it will cause the pH distribution to be disordered, thereby generating concentration polarization and hindering the removal of pollutants.

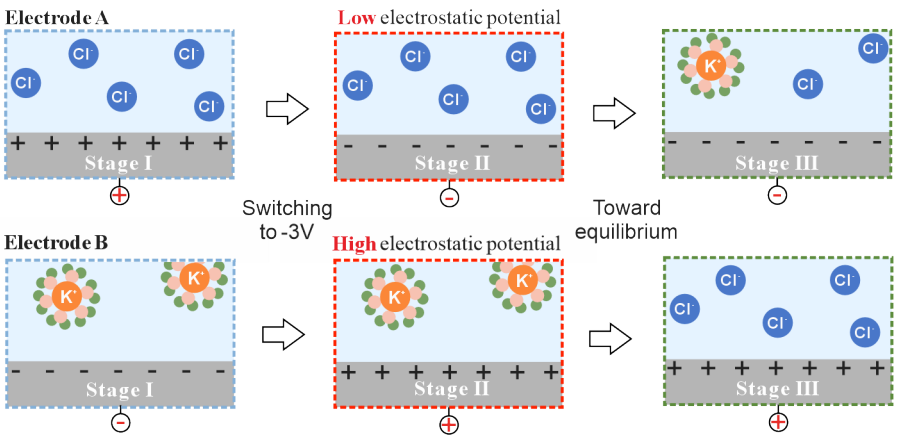

Supplementary Fig. 35 Dynamic process of the electric double layer in single-chamber cell.

Supplementary Note 8. Dynamic process of single-chamber cell

In single-chamber cell, homogeneous solution mixing leads to uniform pH distribution in the single-chamber cell, present relatively neutral environments. For K^+, when pH<7.95, K^+ existing in a hydrated form[10] with more slowly diffusion coefficients and block H^+ into the electric double layer[11].When discharge, the B electrode surface EDL consisting of Cl^- and produce more of the active chlorine or chlorine compounds.

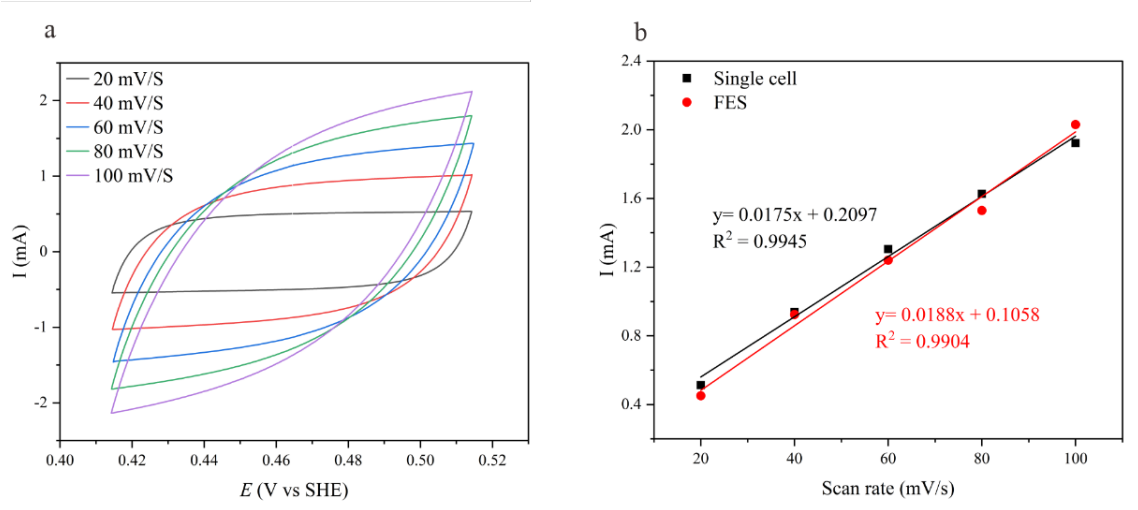

Supplementary Fig. 36 Electric Double layer capacitance. (Single-chamber cell: 0.0175 C, FES: 0.0188 C)

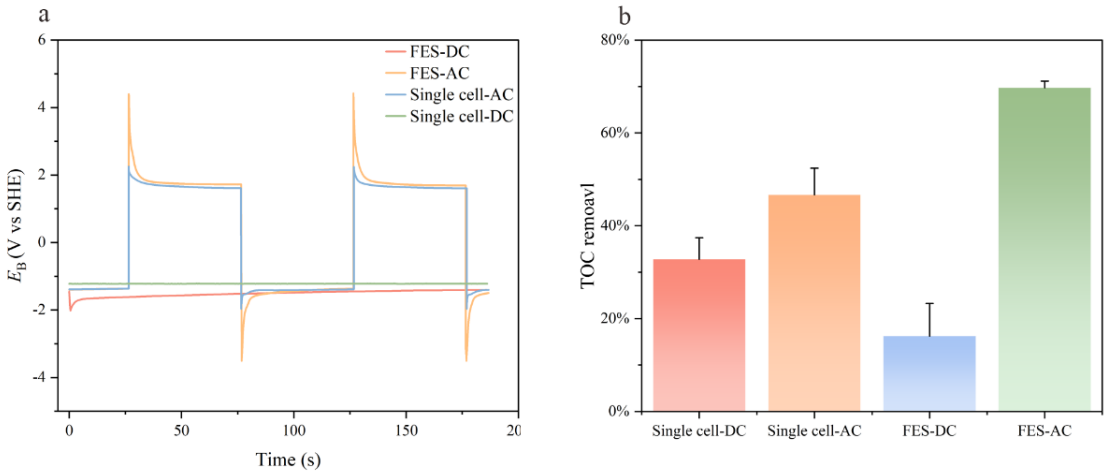

Supplementary Fig. 37 The potential of B electrode (a) and TOC removal (b) under different configurations.

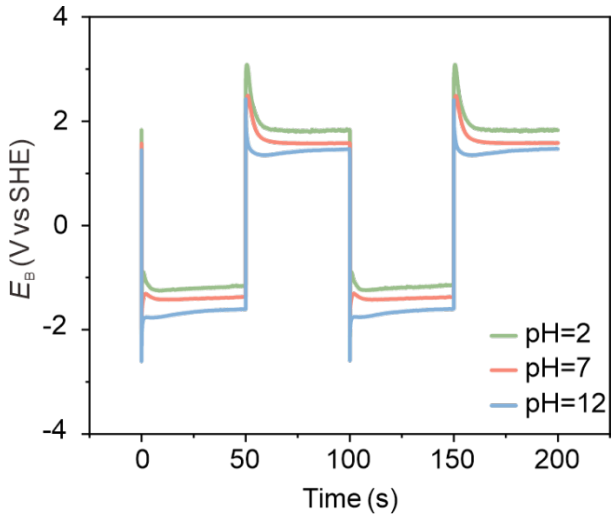

Supplementary Fig. 38 Absolution potential of electrode B under different initial pH solution.

a

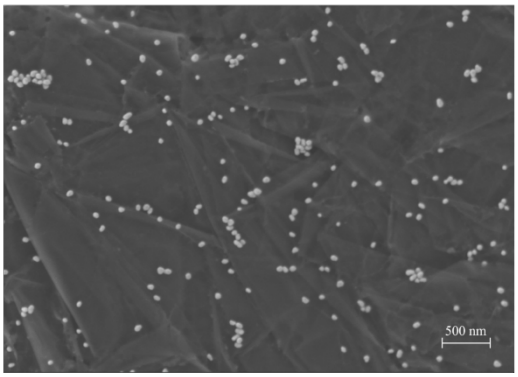

b

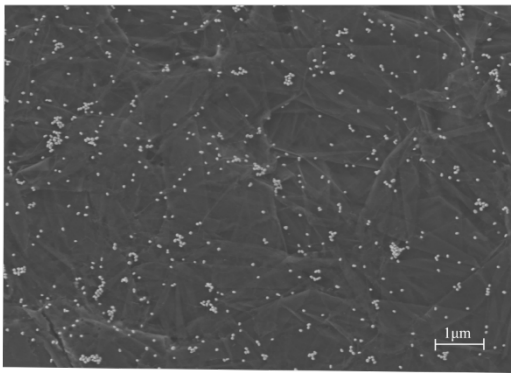

Supplementary Fig. 39 SEM image of shell-isolated nanoparticle-enhanced Raman spectroscopy (SHINERS) on graphite electrode surface.

a

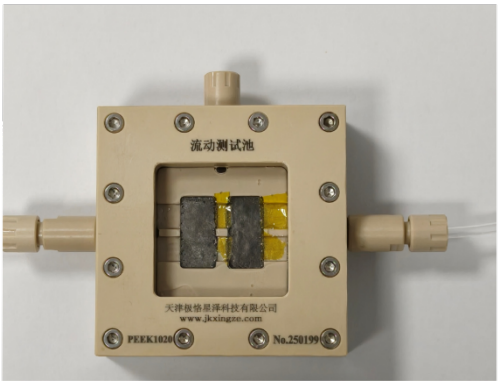

b

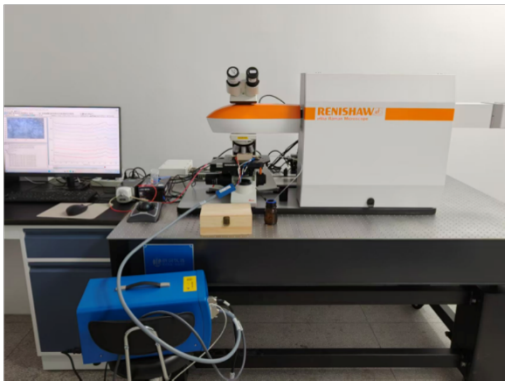

Supplementary Fig. 40 Setup of operando Raman device. (a) Schematic of the operando Raman electrochemical cell. (b) Image of operando electrochemical Raman spectroscopy.

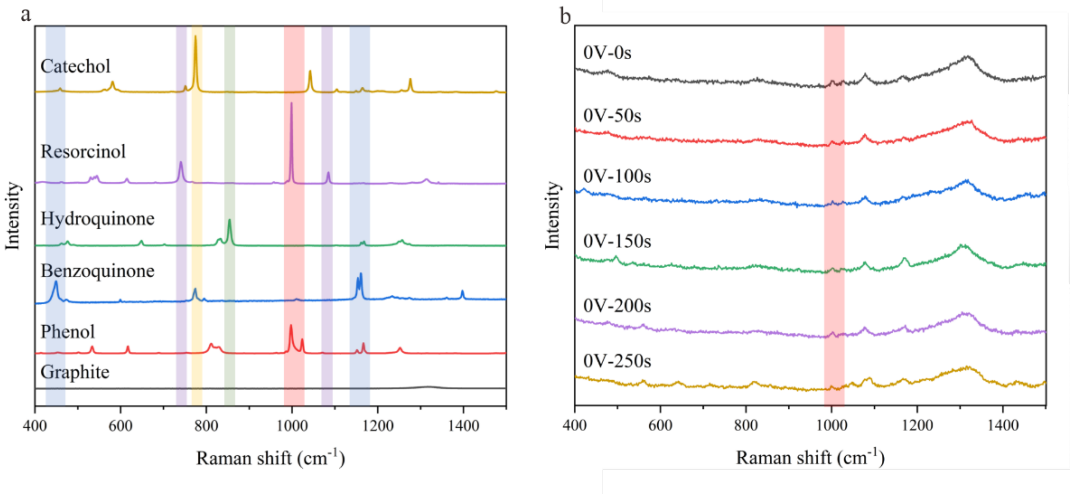

Supplementary Fig. 41 Supplementary Raman spectrum. (a)Raman spectra of phenol and its representative oxidation products. (b)The time series of the Raman spectrum of phenol under 0 V.

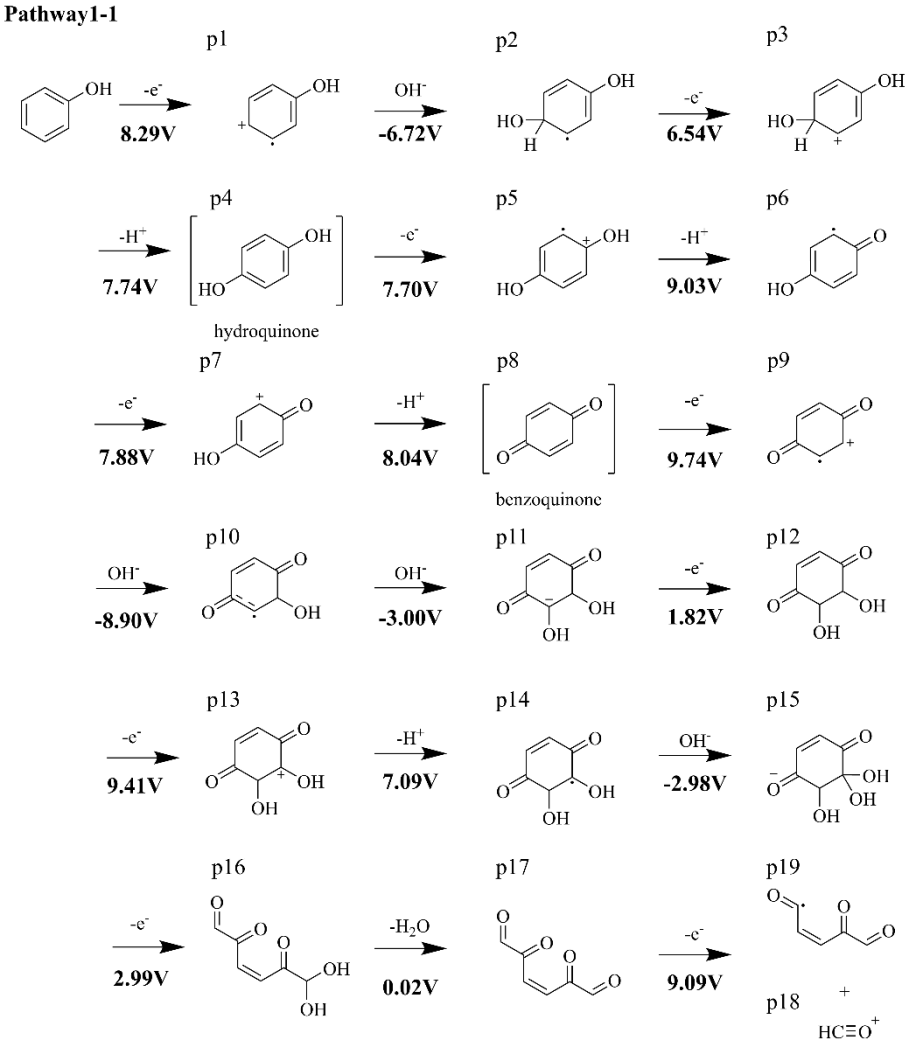

Supplementary Fig. 42 Phenol mineralization pathway and Gibbs free energy.

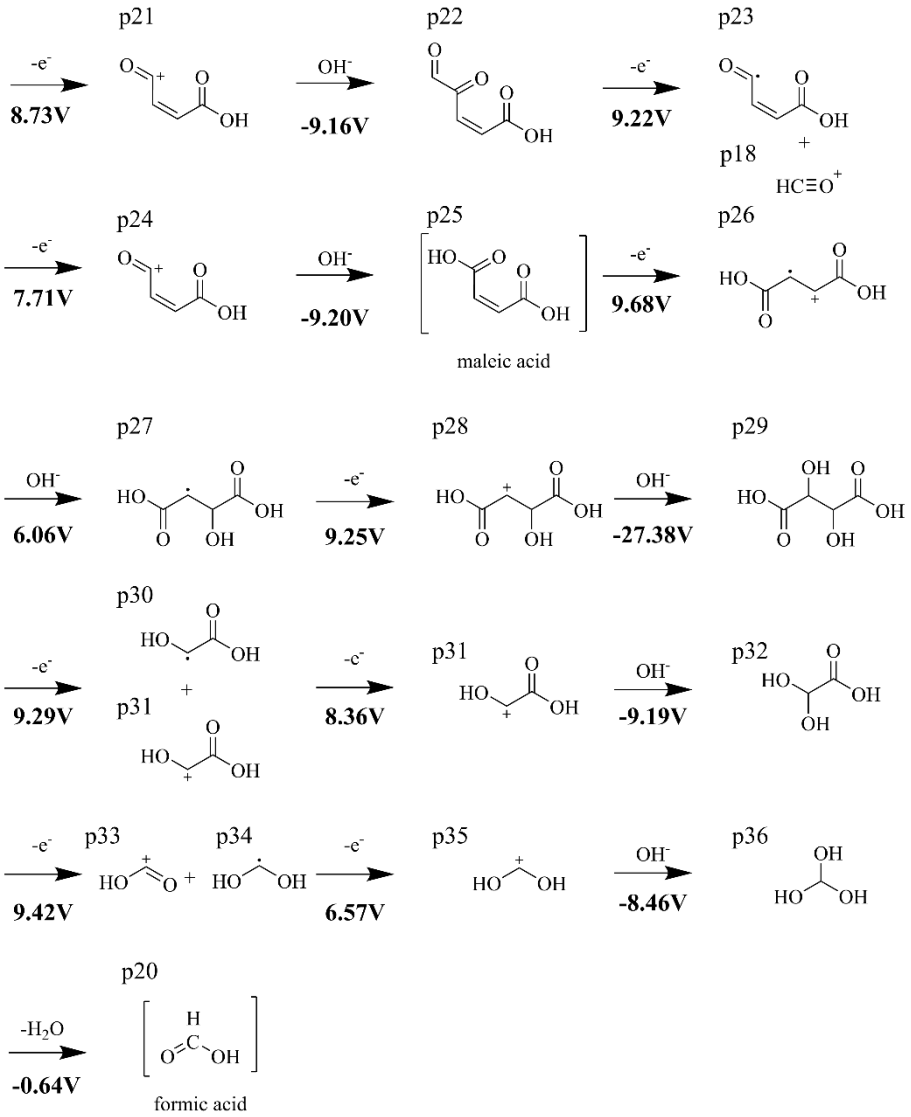

Supplementary Fig. 42 (continued) Phenol mineralization pathway and Gibbs free energy.

Pathway1-2

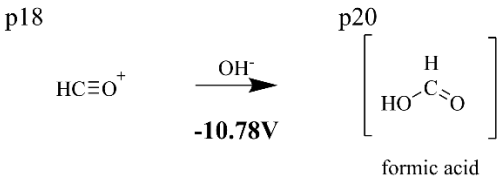

Pathway1-3

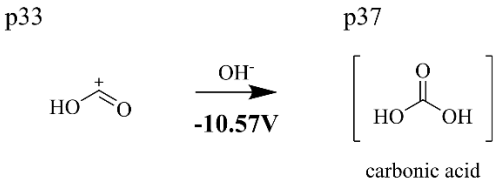

Pathway1-4

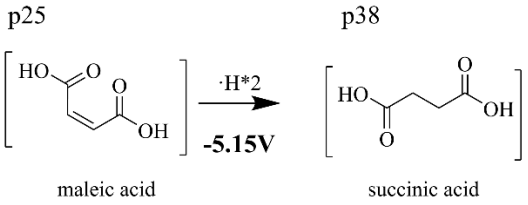

Supplementary Fig. 42 (continued) Phenol mineralization pathway and Gibbs free energy.

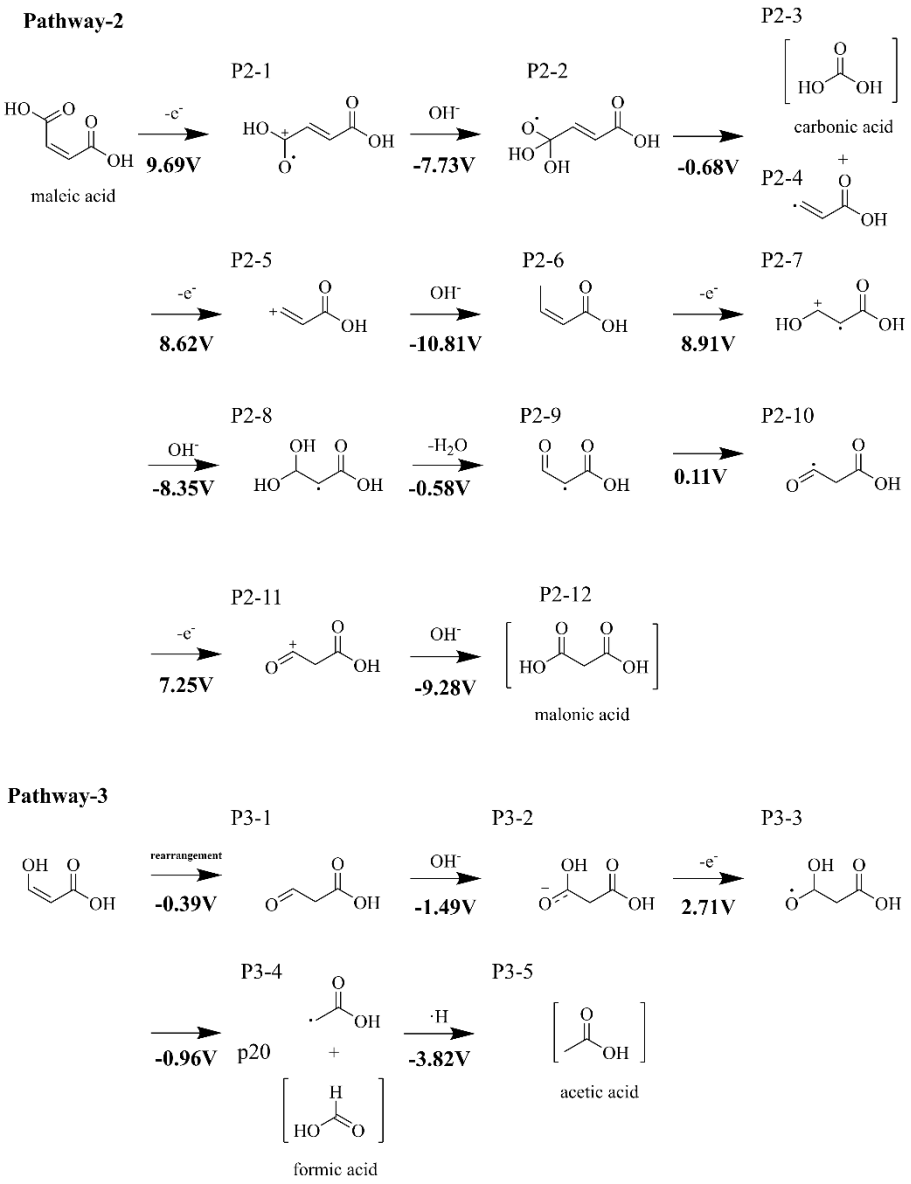

Supplementary Fig. 42 (continued) Phenol mineralization pathway and Gibbs free energy.

Supplementary Table 1 Parameter of COMSOL in diffusion time calculation.

Parameter	Value
Phenol diffusion coefficient	1.01×10^{-9} m^2 s^{-1}
Electrolyte region thickness	110 μm
Phenol initial concentration	0.106 mol m^{-3}
Simulated total time	10 ms
Current density	136 A m^{-2}
Faraday constant	96485 C mol^{-1}

Supplementary Table 2 Parameter of Multiphysics simulation of electrolyte pH.

Parameter	Value
Specific surface area	83300 m^2 m^{-3}
Reference exchange current density	3×10^{-4} A m^{-2}
Anodic transfer coefficient	0.5
Electrolyte flow rate	0/0.2/1/5 mL min^{-1}
Initial potential	0 V
Double-layer capacitance of porous electrode	0.188 F m^{-2}
Initial H^+ concentration	$10^{-2.8}$ mol m^{-3}
Initial OH^- concentration	$10^{-5.2}$ mol m^{-3}
Initial K^+ concentration	100 mol m^{-3}
Initial Cl^- concentration	100 mol m^{-3}
H^+ diffusion coefficient	9.31×10^{-9} m^2 s^{-1}
OH^- diffusion coefficient	5.27×10^{-9} m^2 s^{-1}
K^+ diffusion coefficient	1.96×10^{-9} m^2 s^{-1}
Cl^- diffusion coefficient	1.00×10^{-9} m^2 s^{-1}

Supplementary Table 3 Frequency settings for AC applications in organic pollutant removal.

Target Pollutant	Frequency	Reference
Sulfamethoxazole	4 kHz	[12]
Sulfamethoxazole	4 kHz	[13]
Dye wastewater	2-5 kHz	[14]
Indigo carmine	3-7 kHz	[15]
Ciprofloxacin	100 Hz	[16]
Phenol	10-210 Hz	[17]
Phenol	5 Hz	[1]

Supplementary Table 4 Kramers-Kronig analysis of the data in Supplementary Fig. 33.

Name	EIS data	Residuals
Single-0 rpm	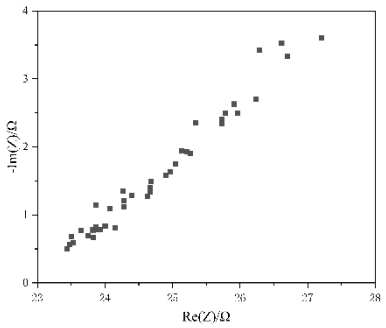	$\chi^2\ (Z) = 3.17e^{-5}$ $\chi^2\ (Z') = 1.15e^{-5}$ $\chi^2\ (-Z'') = 2.02e^{-5}$
Single-200 rpm	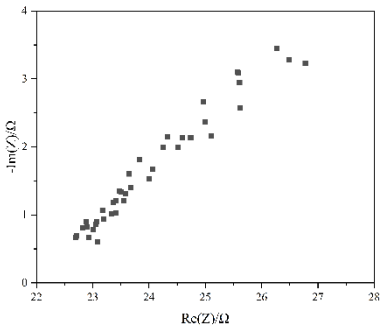	$\chi^2\ (Z) = 3.47e^{-5}$ $\chi^2\ (Z') = 1.69e^{-5}$ $\chi^2\ (-Z'') = 1.78e^{-5}$
FES-1 mL min^{-1}	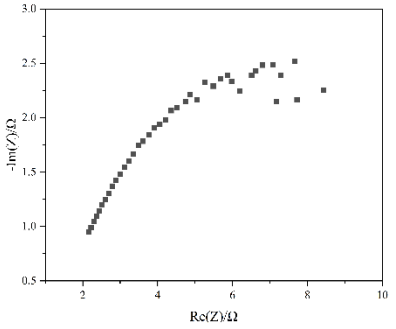	$\chi^2\ (Z) = 1.18e^{-4}$ $\chi^2\ (Z') = 5.53e^{-5}$ $\chi^2\ (-Z'') = 6.33e^{-5}$
FES-5 mL min^{-1}	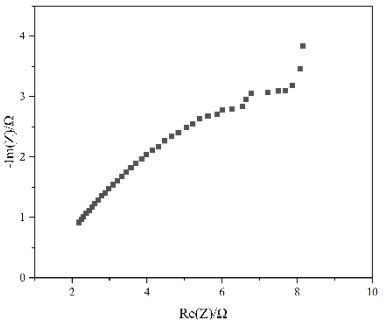	$\chi^2\ (Z) = 1.16e^{-4}$ $\chi^2\ (Z') = 3.31e^{-5}$ $\chi^2\ (-Z'') = 8.35e^{-5}$

Supplementary Table 5 List of assumptions and costs for treating 1 m^3 of wastewater. Using five different advanced oxidation processes (AOPs): ozone oxidation[18], Fenton[19], Electron Fenton[19], electro-oxidation[19], and this work.

AOPs	Classification	Items	Unit	Amount	Unit-price (US \$ ton^{-1} or \$ m^{-3})	Cost (US\$)
Ozone oxidation	Chemical	NaOH	kg	1.00	403.50	0.40
	Electricity	Operation of ozone generator	kWh	1144.00	0.07	80.08
	Total					80.48
Fenton	Chemical	$FeSO_4·7H_2O$	kg	4.69	68.33	0.32
		H_2O_2	kg	34.91	304.76	10.64
		30% NaOH	kg	0.35	414.77	0.15
	Post-treatment	H_2SO_4	kg	0.45	170.14	0.08
		Transportation	t·km	1.20	0.55	0.66
	Total					11.84
Electron Fenton	Chemical	Na_2SO_4	kg	12.40	109.33	1.36
	Electricity	Operation	kWh	65.64	0.07	4.59
	Electrode	Catalyzer	g	50.00	1175.29	0.06
	Post-treatment	Transportation	t·km	0.37	0.55	0.21
	total					6.21
Electron-oxidation (BDD)	Chemical	Na_2SO_4	kg	12.40	109.33	1.36
	Electricity	Electricity	kWh	143.51	0.07	10.05
	Electrode	Catalyzer	g	50.00	1175.29	0.06
		Tantalum	g	7.72	1214.65	0.01
	Post-treatment	Transportation	t·km	0.37	0.55	0.21
	total					11.68

This work	Chemical	KCl	kg	7.46	98.00	0.73
	Electricity	Electricity	kWh	0.27	0.07	0.02
	Electrode	Titanium net	m^2	0.01	3.99	0.05
		Carbon felt	m^2	0.01	45.00	0.60
	total					1.40

For ozone oxidation, we choose 4-Chlorophenol as pollutant, which is similar with phenol[18].

Reference

1 Pei, S., You, S. & Zhang, J. Application of pulsed electrochemistry to enhanced water decontamination. *ACS ES&T Eng.* **1**, 1502-1508, (2021).

2 Martins, L. F. G., Parreira, M. C. B., Ramalho, J. P. P., Morgado, P. & Filipe, E. J. M. Prediction of diffusion coefficients of chlorophenols in water by computer simulation. *Fluid Phase Equilib.* **396**, 9-19, (2015).

3 Niesner, R. & Heintz, A. Diffusion Coefficients of Aromatics in Aqueous Solution. *J. Chem. Eng. Data* **45**, 1121-1124, (2000).

4 Zhao, J. *et al.* Application of UV/O_3/PS coupling process in the treatment of phenol wastewater. *Chinese Journal of Environmental Engineering* **17**, 71-81, (2022).

5 Kusic, H., Koprivanac, N. & Bozic, A. L. Minimization of organic pollutant content in aqueous solution by means of AOPs: UV- and ozone-based technologies. *Chem. Eng. J.* **123**, 127-137, (2006).

6 Xue, T. *et al.* Synergistic degradation of phenol in water by ozone and peroxymonosulfate with interfacial $CoAl_2O_4$@γ-Al_2O_3 catalyst. *J. Water Process. Eng.* **71**, 107298, (2025).

7 Wu, J. *et al.* Enhancing oxidative capability of Ferrate(VI) for oxidative destruction of phenol in water through intercalation of Ferrate(VI) into layered double hydroxide. *Appl. Clay Sci.* **171**, 48-56, (2019).

8 Tian, S. *et al.* Insight into the oxidation of phenolic pollutants by enhanced permanganate with biochar: The role of high-valent manganese intermediate species. *J. Hazard. Mater.* **430**, 128460, (2022).

9 Ni, X.-Y. *et al.* Enhancing disinfection performance of the carbon fiber-based flow-through electrode system (FES) by alternating pulse current (APC) with low-frequency square wave. *Chem. Eng. J.* **410**, 128399, (2021).

10 Singh, M. R., Kwon, Y., Lum, Y., Ager, J. W. & Bell, A. T. Hydrolysis of electrolyte cations enhances the electrochemical reduction of CO_2 over Ag and Cu. *J. Am. Chem. Soc.* **138**, 13006-13012, (2016).

11 Gu, J. *et al.* Modulating electric field distribution by alkali cations for CO_2 electroreduction in strongly acidic medium. *Nat. Catal.* **5**, 268-276, (2022).

12 Wang, J., Wang, A., Song, J., Zhang, I. Y. & Huang, R. A sustainable electrochemical strategy utilizing pulsed alternating current and dual carbon felt electrodes for enhanced degradation of organic pollutants: Oxidation performance and mechanisms. *J. Environ. Chem. Eng.* **12**, 112999, (2024).

13 Wang, J., Long, X., Zhang, I. Y. & Huang, R. Pulsed versus direct current electrochemical co-catalytic peroxymonosulfate-based system: Elevated degradation and energy efficiency with enhanced oxidation mechanisms. *J. Hazard. Mater.* **458**, 132004, (2023).

14 Wang, J. *et al.* Multivariate optimization of the pulse electrochemical oxidation for treating recalcitrant dye wastewater. *Sep. Purif. Technol.* **230**, 115851, (2019).

15 Ren, W. *et al.* Electro-induced carbon nanotube discrete electrodes for sustainable persulfate activation. *Environ. Sci. Technol.* **56**, 14019-14029, (2022).

16 Zhou, T. *et al.* The process and mechanism of pulse electrolytic oxidation of ciprofloxacin antibiotic in wastewater on boron-doped diamonds. *Process Saf. Environ. Protect.* **173**, 452-460, (2023).

17 Wei, J., Zhu, X. & Ni, J. Electrochemical oxidation of phenol at boron-doped diamond electrode in pulse current mode. *Electrochim. Acta* **56**, 5310-5315, (2011).

18 Cañizares, P., Paz, R., Sáez, C. & Rodrigo, M. A. Costs of the electrochemical oxidation of wastewaters: a comparison with ozonation and Fenton oxidation processes. *J. Environ. Manage.* **90**, 410-420, (2009).

19 Chen, K.-Y. *et al.* Biological waste-derived dual-site catalyst empowers electro-fenton systems to sustainably decontaminate livestock wastewater. *ACS ES&T Eng.* **4**, 3057-3066, (2024).